JOM, Vol. 68, No. 5, 2016
DOI: 10.1007/s11837-016-1857-6
© 2016 The Minerals, Metals & Materials Society (outside the U.S.)

Direct Numerical Simulations in Solid Mechanics for Quantifying the Macroscale Effects of Microstructure and Material Model-Form Error

JOSEPH E. BISHOP,[1,5] JOHN M. EMERY,[1,6] CORBETT C. BATTAILE,[2,7] DAVID J. LITTLEWOOD,[3,8] and ANDREW J. BAINES[4,9]

1.—Engineering Sciences Center, Sandia National Laboratories, Albuquerque, NM 87185, USA. 2.—Materials Science and Engineering Center, Sandia National Laboratories, Albuquerque, NM 87185, USA. 3.—Computing Research Center, Sandia National Laboratories, Albuquerque, NM 87185, USA. 4.—General Motors Proving Ground, General Motors, 3300 General Motors Rd., Milford, MI 48480, USA. 5.—e-mail: jebisho@sandia.gov. 6.—e-mail: jmemery@sandia.gov. 7.—e-mail: ccbatta@sandia.gov. 8.—e-mail: djlittl@sandia.gov. 9.—e-mail: andrew.baines@gm.com

Two fundamental approximations in macroscale solid-mechanics modeling are (1) the assumption of scale separation in homogenization theory and (2) the use of a macroscopic plasticity material model that represents, in a mean sense, the multitude of inelastic processes occurring at the microscale. With the goal of quantifying the errors induced by these approximations on engineering quantities of interest, we perform a set of direct numerical simulations (DNS) in which polycrystalline microstructures are embedded throughout a macroscale structure. The largest simulations model over 50,000 grains. The microstructure is idealized using a randomly close-packed Voronoi tessellation in which each polyhedral Voronoi cell represents a grain. An face centered cubic crystal-plasticity model is used to model the mechanical response of each grain. The overall grain structure is equiaxed, and each grain is randomly oriented with no overall texture. The detailed results from the DNS simulations are compared to results obtained from conventional macroscale simulations that use homogeneous isotropic plasticity models. The macroscale plasticity models are calibrated using a representative volume element of the idealized microstructure. Ultimately, we envision that DNS modeling will be used to gain new insights into the mechanics of material deformation and failure.

INTRODUCTION

A key challenge for predictive modeling in solid mechanics is upscaling the multitude of inelastic processes occurring at the microscale without filtering emergent phenomena such as strain localization and fracture. Furthermore, any macroscale engineering quantity of interest, used in formulating an engineering decision, should have quantified error/uncertainty due to intrinsic material variability and various sources of modeling error such as homogenization, discretization error in finite-element analysis, and model-form error in constitutive modeling. Engineered structures composed of metallic materials typically contain complex spatially varying polycrystalline microstructures resulting from the manufacturing process. The manufacturing process not only alters the microstructure but also creates a complex spatially varying texture (non-uniformly random crystal orientations).[1,2] This is particularly true for laser-based metal additive manufacturing in which new material is deposited in a melt pool on the preceding layers.[3] The rapidly varying temperature field within the additive process produces an extremely complex microstructure and internal state. For these structures, the quantification of macroscale uncertainty is particularly challenging.

Homogenization theory provides a mathematical basis for upscaling the microstructural response to the macroscale. The fundamental approximation in homogenization theory is that there exists a "scale separation" between the microscale and the

macroscale. The actual scales used in this approximation are problem-dependent. One heuristic definition is that the length scale of the macroscopic geometric feature should be much larger than the average grain size. The scale-separation approximation is crucial to macroscale solid-mechanics modeling since it provides a clear separation between the material, with well-defined objective macroscale properties, and the response of the macroscale structure modeled using continuum mechanics. In cases where the assumption of scale separation is inapplicable, predicting the macroscale response becomes much more difficult as one then needs to embed the material microstructure directly within the macroscale structure.[4–6]

In macroscale constitutive modeling, there are typically several models available that can each be precisely calibrated to available test data, but can differ in their predictions away from the calibration points. For example, for simplicity, many engineering materials are approximated as isotropic, even though they exhibit some degree of anisotropy. To actually distinguish between the two models requires additional tests beyond those required to minimally identify the isotropic parameters. In the plastic regime, even for an isotropic material, there are several types of yield criteria, e.g., Tresca, von Mises,[7] and the Hosford class of yield surfaces.[8] A single tensile test cannot distinguish between the different yield criteria. These types of modeling errors are referred to as "model-form errors."

In an era of petascale computing, and the promise of future exascale computing[9], it is now possible to perform direct numerical simulations (DNS) in solid mechanics, where the microstructure is modeled directly in a macroscale structure.[10] With the dual goals of understanding material variability and quantifying the effect of model-form errors on engineering quantities of interest, we perform a set of direct numerical simulations in which polycrystalline microstructures are embedded throughout a macroscale structure. Ideally, these microstructures and internal state variables would be generated through material process modeling[11] or reconstructed from experimental observations.[12] Here, the microstructure is idealized using a Voronoi tessellation seeded with a maximal Poisson-sampling process.[13] This type of Voronoi construction results in an equiaxed microstructure.[10] Other physically motivated Voronoi constructions are possible.[14] Each Voronoi cell is taken to be a grain with no preferred crystal orientation (no texture). An face centered cubic (FCC) crystal-plasticity model is then used to model the mechanical response of each grain.[15,16]

A voxelation approach is used to embed the microstructure into the macroscale structure.[10] The macroscale structure is discretized with a highly refined finite-element mesh with element sizes several times smaller than the grain size. Each finite element is assigned the properties of the grain containing the centroid of the hexahedral element. This approach to microstructural embedding is simple and robust, unlike an explicit microstructural meshing approach in which degenerate elements are invariably created making it difficult to simulate numerous realizations of the microstructure.[12,17–19]

The largest simulations model over 50,000 grains within a small macroscale structure, a tube with two side-holes loaded in tension. Results from the DNS simulations are compared to those obtained from conventional macroscale simulations that use isotropic rate-independent plasticity. The macroscale plasticity models are calibrated using a representative volume element of the idealized microstructure using homogenization techniques.

This paper is organized as follows. The DNS method for solid mechanics is reviewed in "Direct Numerical Simulation" section. The material and microstructural model are presented in "Material and Microscale Model" section. The process for obtaining the homogenized properties, both in the elastic and plastic regime, is detailed in "Macroscale Material Model" section. The DNS results from the macroscale structure are presented in "Simulation of a Tube with Side-Holes Loaded in Tension: Comparison of DNS and Macroscale Material Models" section, including a comparison of the response of the macroscale structure using both DNS and homogenization. Conclusions and future work are given in "Conclusions" section.

DIRECT NUMERICAL SIMULATION

An approach for directly simulating microstructure within a macroscale structure has been recently proposed by Bishop et al.[10] This methodology is adopted here, and is briefly reviewed in this section. Other methods for microstructural embedding and DNS modeling have been used by other researchers.[6,20,21]

The explicit meshing of polycrystalline grains of general morphology, using a mesh that conforms to the grain boundaries, is challenging and typically requires a certain amount of user intervention. The likelihood of requiring user intervention increases as the number of grains increases. This meshing problem is currently an active area of research.[12,17–19,22,23] Constructing a mesh that is conformal both with the geometry of the macrostructure and microstructure is even more challenging. One goal of this work is to perform direct numerical simulations on a large number of microstructural realizations (an ensemble). Each realization contains many thousands of grains. Thus, a robust discretization approach is needed. For this reason, we adopt an approach in which the macroscale structure is meshed explicitly with hexahedral finite elements, but the microstructure is only pixelated/voxelated (using the same mesh). This is a common technique in the modeling of

composite and polycrystalline microstructures within a representative volume element.[24,25] Pyle et al. have compared the use of a voxelation representation of the grain structure to the use of a conformal tetrahedral mesh in polycrystal simulations.[26] One of their conclusions was that the texture evolution and statistical distribution of stress were similar for both representations, in addition to the mean (macroscopic) behavior. In this work, we are not attempting to resolve the detailed stress and strain fields near the grain boundaries. Instead, we are interested in the mean response within a grain and stress and strain fluctuations above the grain scale induced by the grain structure. With this goal in mind, a voxel representation of the grain structure is deemed sufficient.

To model the microstructure directly within a macroscale structure, we leverage high-performance computing resources and use a finite-element mesh that is fine enough to resolve the microstructural detail. A volume of 1 cm^3 containing 125-μm-sized grains contains approximately 512,000 grains. The direct numerical simulation of the microstructure within this volume requires many millions of finite elements to sufficiently resolve the grain structure. The use of such a highly refined mesh requires massively parallel finite-element software and for an implicit solution, an equation solver that can scale to thousands of processors. In this work, we use the implicit solid mechanics module within the Sierra multiphysics finite-element software suite[27] and the FETI-DP solver. FETI-DP is a domain-decomposition iterative solver that uses Lagrange multipliers to enforce compatibility at the subdomain interfaces.[28]

For an example of the DNS modeling approach, consider the round-bar tension specimen shown in Fig. 1a. First, a coarse conformal hexahedral mesh of the macroscale structure is created as shown in Fig. 1b. This base mesh is referred to as the $r0$-mesh refinement. Subsequent hexahedral mesh refinements, $r1$, $r2$, $r3$,… are obtained through uniform hierarchical refinement in which each hexahedron is divided into eight hexahedra. New surface nodes created during each refinement are located on the exact macroscale geometry. Figure 1c shows the $r1$-mesh refinement. The hierarchical refinement is continued until the element size is sufficiently small to resolve each grain to the desired level of accuracy. In this work, the meshing tool CUBIT[29] was used to create both the geometry and hexahedral meshes.

Next, a bounding box of the macroscale structure is created. The model microstructure is then created within this bounding box. This is demonstrated in Fig. 2 using only the gauge section of the round-bar tension specimen. The model microstructure is the idealized equiaxed Voronoi microstructure developed in "Material and Microscale Model" section. Each finite element is assigned to a specific grain based on the location of the centroid of the hexahedral element. The resulting grain imprinting is shown in Fig. 3 for several levels of mesh refinement. For this example, there are approximately six grains through the diameter of the gauge section. The base $r0$ hexahedral mesh barely resolves the grain structure with one element per grain, approximately. Mesh refinements $r1$ through $r4$ resolve the grain structure with approximately 2^3, 4^3, 8^3, and 16^3 hexahedral elements per grain, respectively. The grain structure begins to emerge at the $r2$ level of mesh refinement, and is clearly discernible at higher levels of mesh refinement, $r3$ and $r4$.

There is a trade-off between modeling as many grains as possible within the macroscale structure (resulting in a smaller number of hexahedral elements per grain) and minimizing the finite-element discretization error (resulting in a larger number of hexahedral elements per grain). As shown in "Macroscale Material Model" section, a mesh refinement level in which there are approximately 8^3 hexahedral elements per grain (three levels of mesh refinement beyond the first mesh that resolves the grain structure) sufficiently minimizes the finite-element discretization error for present purposes. This will be referred to as a "+3" level of mesh refinement with respect to the grain structure. The example in Fig. 3d corresponds to a +3 mesh refinement. This level of relative mesh refinement will be used in the example presented in "Simulation of a Tube with Side-Holes Loaded in Tension: Comparison of DNS and Macroscale Material Models" section.

MATERIAL AND MICROSCALE MODEL

The material modeled in this study is AISI 304L stainless steel. This material possesses an austenitic (γ-Fe) microstructure and an FCC crystal system. A micrograph is shown in Fig. 4a. The microstructural model is presented in "Microstructural Model" section. The crystal plasticity model is reviewed in "Crystal-Plasticity Model" section.

Microstructural Model

Ideally, the full three-dimensional grain structure, texture, and internal hardening state of the material would be obtained through a combination of direct measurement and process modeling that included the full manufacturing history. This level of capability in both modeling and experimental characterization is the vision of Integrated Computational and Materials Engineering (ICME).[30] Here, we do not perform any type of process modeling, but rather assume an initial textureless equiaxed microstructure. A thermodynamically consistent microstructure could be derived using phase-field modeling[14,31] or kinetic Monte Carlo,[11,32,33] for example, or other thermodynamically motivated techniques.[34] For efficiency and robustness, here we use an idealized microstructure derived from a classical Voronoi tessellation. The particular Voronoi construction used in this work is detailed in the work of Bishop et al.,[10] and is briefly reviewed here,

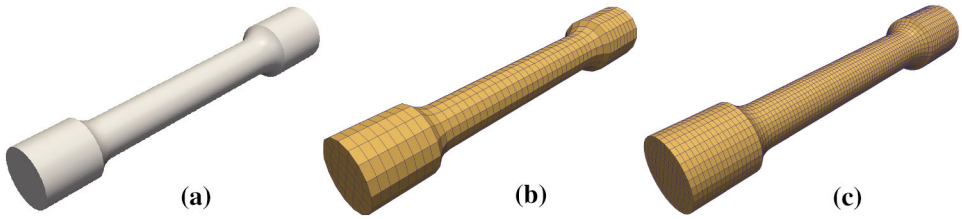

Fig. 1. (a) Example structure, a round-bar tension specimen. (b) Base hexahedral mesh denoted as $r0$. (c) Subsequent hexahedral meshes, $r1, r2, r3, \ldots$ are obtained from uniform hierarchical refinement in which each hexahedron is divided into eight. New surface nodes created during each refinement are located on the exact geometry. Here, $r1$ is shown. (Reproduced with permission from Ref. 10).

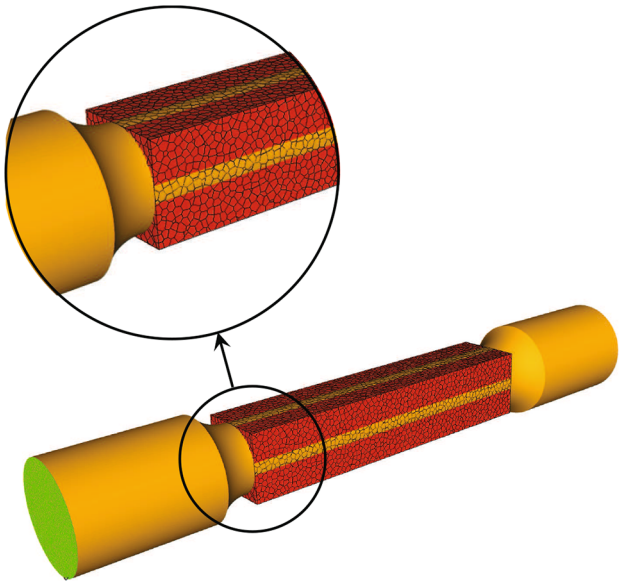

Fig. 2. Imprinting of a microstructure onto a macroscopic structure, here the gauge section of the round-bar tension specimen shown in Fig. 1. The bounding box enclosing the gauge section is first tessellated using the Voronoi structure shown in Fig. 4. The microstructural imprinting is done implicitly by identifying the Voronoi cell that contains a given hexahedral centroid. The results are shown in Fig. 3. (Reproduced with permission from Ref. 10).

although other physically motivated Voronoi constructions are possible.[14] While a Voronoi tessellation can be formed from any finite set of points or seeds, a special structure arises from the close packing of equisized hard spheres, called random close-packing (RCP). The RCP structure is realized by a spatial sampling process known as maximal Poisson disk sampling (MPS). This seeding process and subsequent Voronoi construction are demonstrated in Fig. 4b–d. For the RCP structure, the average aspect ratio of each Voronoi cell is approximately one. Thus, the RCP Voronoi structure provides an equiaxed grain structure. Note that the faces of each Voronoi cell are planar, while for a physical grain they are generally non-planar.

Each Voronoi cell is taken to represent a single grain. The initial crystal orientation within a grain is taken to be uniform. The orientation of each grain is taken to be an independent, identically distributed, random variable with no preferred orientation (no texture). Care is needed in randomly assigning the grain orientations to actually realize a no-texture state (see, for example, Refs. 35 and 36). In the absence of a crystal texture, the *initial* homogenized mechanical response of the material is isotropic. The effective mechanical properties of this material structure will be discussed in detail in "Macroscale Material Model" section.

Crystal-Plasticity Model

The mechanical response of each FCC grain is modeled using an elasto-viscoplastic crystal-plasticity model developed by Maniatty et al.[2,15,16] This model is partially reviewed here with relevant material parameters defined.

For the elastic response, the austenite FCC crystal structure possesses cubic symmetry with elastic constants $C_{11} = 204.6\text{GPa}$, $C_{12} = 137.7\text{GPa}$, and $C_{44} = 126.2\text{GPa}$.[37] The anisotropy ratio A for this crystal is $A = 2C_{44}/(C_{11} - C_{12}) = 3.77$, which is relatively large. For an isotropic material, $A = 1$.

The plastic velocity gradient L^p is given by

$$L^p = \sum_{\alpha=1}^{12} \dot{\gamma}^\alpha P^\alpha \,, \tag{1}$$

where $\dot{\gamma}^\alpha$ is the rate of plastic shear on the α slip system, and P^α is the Schmid tensor defined as

$$P^\alpha = m^\alpha \otimes n^\alpha \,, \tag{2}$$

where n^α and m^α are the slip plane normal and slip direction of the α slip system, respectively. The summation in Eq. 1 is over each of the 12 FCC slip systems.

The plastic shear rate $\dot{\gamma}^\alpha$ on slip system α is modeled as

$$\dot{\gamma}^\alpha = \dot{\gamma}_0 \left| \frac{\tau^\alpha}{g^\alpha} \right|^{1/m} sign(\tau^\alpha) \,, \tag{3}$$

where τ^α is the resolved shear stress on slip system α, g^α is the slip system hardness, $\dot{\gamma}_0$ is the reference plastic shear rate, and m is the material rate sensitivity. Smaller values of m result in a less rate-sensitive material response.

Within the Voce–Kocks model of work hardening, all slip systems harden at the same rate and start with the same hardness. Under this assumption, the superscript α can be dropped from g^α. The hardness evolution is modeled as

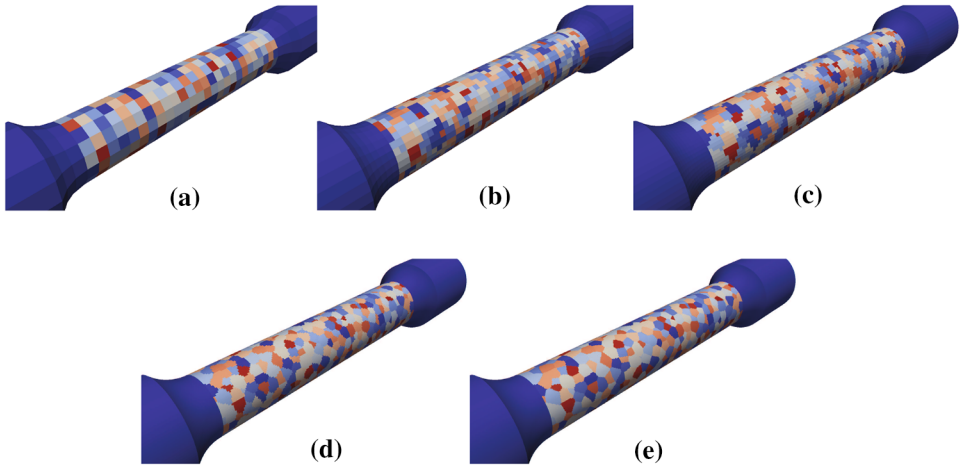

Fig. 3. A succession of refined hexahedral meshes illustrating the resolution of the grain structure. There are approximately six grains through the diameter of the gauge section of the round-bar specimen. (a) Base *r*0 hexahedral mesh with approximately 1 hexahedral element per grain. (b)–(e) Mesh refinements *r*1 through *r*4 with approximately 2^3, 4^3, 8^3, and 16^3 hexahedral elements per grain, respectively. The relative mesh refinement shown in case (d) is used for all results presented in this paper (Reproduced with permission from Ref. 10).

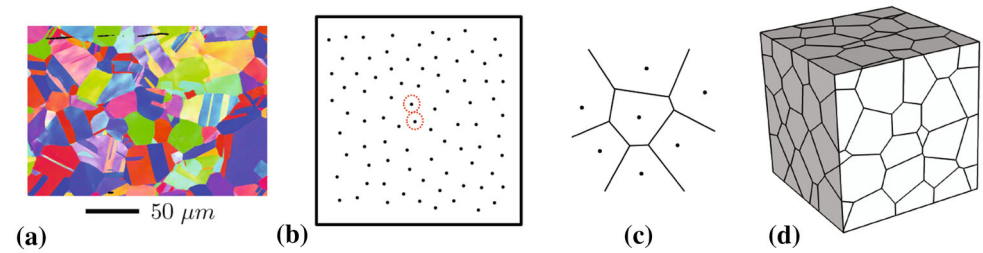

Fig. 4. (a) Grain structure of wrought 304L stainless steel identified through electron backscatter diffraction (EBSD). (b) Random close-packing of a 2D region also known as maximal Poisson disk sampling (MPS). Two exclusion disks are identified. (c) Voronoi diagram of a set of points in the plane. (d) Voronoi tessellation of a 3D region after MPS sampling. (Reproduced with permission from Ref. 10).

$$\dot{g} = G_0 \left(\frac{g_s - g}{g_s - g_0} \right) \dot{\gamma} \,, \tag{4}$$

where G_0 is the hardening rate, g_0 is the initial resolved shear strength, and $\dot{\gamma}$ is the total plastic shear rate on all slip systems defined as

$$\dot{\gamma} = \sum_{\alpha=1}^{12} |\dot{\gamma}^{\alpha}| \,. \tag{5}$$

The saturation value of the hardness g_s is given by

$$g_s = g_{s_0} \left| \frac{\dot{\gamma}}{\dot{\gamma}_s} \right|^{\omega} , \tag{6}$$

where g_{s_0}, $\dot{\gamma}_s$, and ω are material parameters. In this work, we take $\omega = 0$ so that $g_s = g_{s_0}$. The values of the remaining material parameters are given in Table I. These parameter values result in a plastic response that is *representative* of 304L in the small strain regime. More sophisticated hardening models, both self and latent, are available in the literature but are not explored here.[38–40]

MACROSCALE MATERIAL MODEL

Our goal in this section is to develop a homogenized, macroscale, material model, in both the elastic and plastic regimes, for the polycrystalline material presented in "Material and Microscale Model" section. By construction, the model microstructure defined in "Microstructural Model" section is homogeneous and isotropic (at least initially) at the macroscale. The homogenized *elastic* properties of the model microstructure were previously obtained by Bishop et al. using a limiting process based on representative volume elements.[10] The effective Young's modulus and Poisson's ratio are 197.6 GPa and 0.294, respectively. For the homogenized plastic response, a concurrent computational homogenization approach has been proposed by Kouznetsova et al.[41,42] Here, we *approximate* the homogenized plastic behavior using two macroscale, rate-independent, isotropic, plasticity models: (1) one that uses the von Mises yield surface,[7] and (2) another that uses the more general Hosford yield surface.[8] Each plasticity model assumes isotropic hardening in stress space.

Table I. Material parameters used in the crystal-plasticity model, Eqs. 3–6

Parameter	Value	Units
m	0.01	–
$\dot{\gamma}_0$	0.01	1 / s
G_0	465	MPa
g_0	130	MPa
g_{s_0}	230	MPa
ω	0	–

Representative Volume Element

In order to identify the parameters in the macroscale plasticity models, we use a representative volume element (RVE) approach. First, we need to identify a sufficiently large volume of grains so that the macroscale properties are independent of both the size of the volume and the boundary conditions applied to the volume (uniform tractions or displacements). If the microstructure were periodic, periodic boundary conditions could be applied to a unit cell to calculate the homogenized material properties following the standard asymptotic homogenization procedure.[43–46] For the present random polycrystalline microstructure, in which a periodic unit cell does not exist, the homogenized material properties must be obtained from a limiting process in which increasingly larger sample sizes are considered.[10] This limiting process is necessary to obtain unique material properties that are not dependent upon the boundary conditions applied to the sample of material. Second, we need to identify a level of mesh refinement for each grain so that the macroscale properties are insensitive to further mesh refinement.

To understand the importance of choosing a representative volume size, consider a sequence of increasingly larger material volumes (samples), and thus an increasing number of grains, each with geometric similitude. Each sample volume and microstructural realization is called a stochastic volume element (SVE),[47] since the apparent material properties are inherently stochastic. Only in the limit of an infinitely large SVE do these *apparent* material properties become independent of the boundary conditions applied to the SVE (e.g., statically uniform tractions, kinematically uniform displacements, or periodic displacements). The resulting unique material properties are called *effective* material properties. These properties are deterministic. Any SVE of finite size, but sufficiently large with *apparent* material properties approximately equal to the *effective* material properties, is called a representative volume element (RVE). The appropriate RVE size and the convergence behavior of the *apparent* material properties to the *effective* material properties have been studied extensively in the literature,[24,48–52] although mostly in the elastic regime. The terms *apparent* and *effective* material properties were defined by Huet in his proof of the Partition Theorem.[53]

In order to choose an appropriate RVE size and finite-element mesh refinement, a hierarchy of three SVE volumes is considered. The smallest volume contains approximately 4^3 grains. Subsequent volumes are obtained by doubling the dimensions resulting in 8 times the volume and approximately 8 times as many grains as the previous SVE size. Thus, the second SVE size contains approximately 8^3 grains, and the third SVE size approximately 16^3 grains. (Note that the crystal-plasticity model described in "Crystal-Plasticity Model" section has no inherent length scale. Thus, the physical size of the grains is not significant, but only the number of grains per unit of volume.)

For the finite-element discretization of each SVE, the voxelation paradigm described in "Direct Numerical Simulation" section is used. The smallest volume (containing approximately 4^3 grains) is meshed uniformly with 16^3 hexahedral elements resulting in approximately 4^3 elements per grain. This level of mesh refinement will be referred to as the "+2 mesh", since the level of mesh refinement is two hierarchical levels above the mesh resolution that just resolves a grain (with 1^3=1 element). There are 8 times as many finite elements for each subsequent refinement in the sequence, and therefore 8 times as many hexahedral elements per grain. Thus, there are approximately 8^3 elements per grain in the +3 mesh and approximately 16^3 elements per grain in the +4 mesh. This hierarchy of SVE sizes and finite-element mesh resolutions is shown in Fig. 5.

For the following SVE/RVE simulations, either statically uniform normal tractions or kinematically uniform displacement boundary conditions are applied to the faces of an SVE in order to reproduce the desired mean stress state or strain state. In the absence of body forces or imperfect interfaces, the volume-averaged Cauchy stress $\langle\sigma\rangle$ in the deformed configuration is related to the surface tractions by the relationship[54]

$$\langle\sigma\rangle \doteq \frac{1}{v}\int_v \sigma \, dv = \frac{1}{v}\int_{\Gamma_v} x \otimes t \, d\Gamma_v \,, \tag{7}$$

where v is the volume of the SVE in the deformed configuration, x is the position vector in the deformed configuration, t is the surface traction vector, and Γ_v represents the surface of the RVE in the deformed configuration. In the absence of internal surface discontinuities or voids, the volume-averaged deformation gradient $\langle F\rangle$ in the undeformed configuration is given by[54]

$$\langle F\rangle \doteq \frac{1}{V}\int_V F \, dV = \frac{1}{V}\int_{\Gamma_V} x \otimes N \, d\Gamma_V \tag{8}$$

where V is the volume of the SVE in the undeformed configuration, and N is the surface normal in the undeformed configuration.

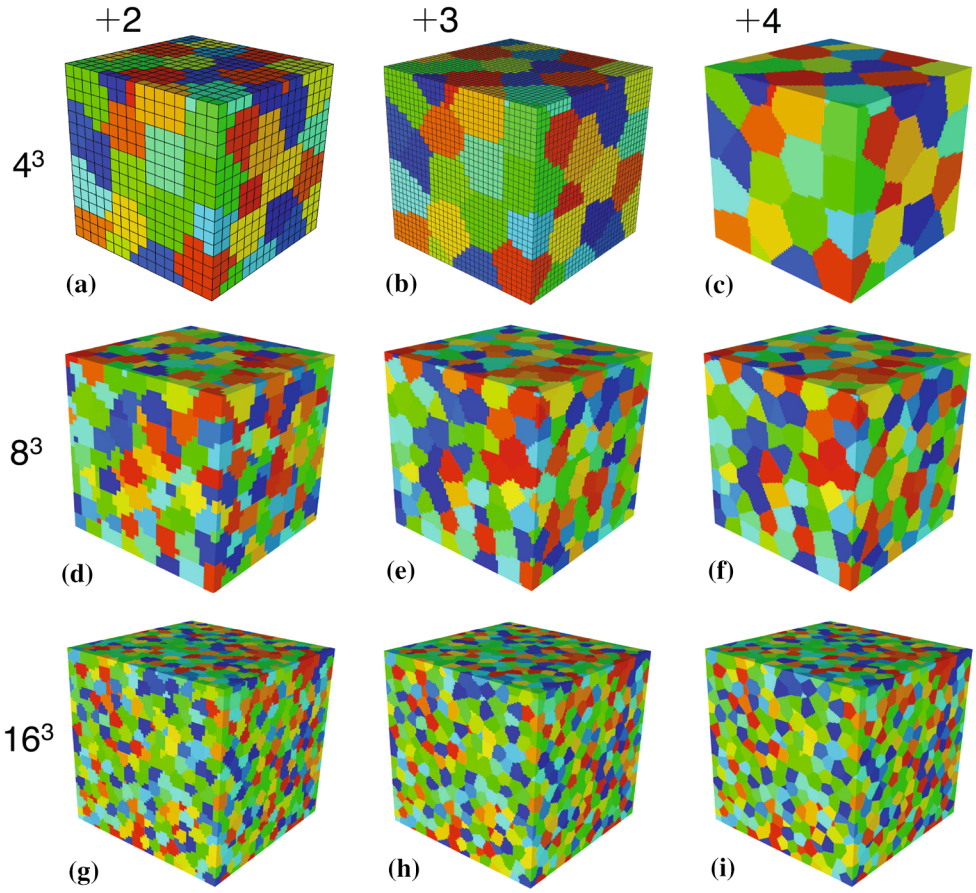

Fig. 5. Three stochastic volume elements (SVEs) of increasing size, and thus with increasing numbers of grains, and increasing levels of mesh refinement: (a–c) approximately 4^3 grains, (d–f) approximately 8^3 grains, and (g–i) approximately 16^3 grains. Three levels of mesh refinement are shown for each SVE size: (a, d, g) approximately 4^3 elements per grain (+2 mesh), (b, e, h) approximately 8^3 elements per grain (+3 mesh), and (c, f, i) approximately 16^3 elements per grain (+4 mesh). These SVEs are used to determine an appropriate RVE size and level of mesh refinement. (The color of each grain is arbitrary, and does not indicate crystal orientation).

Given the volume-averaged deformation gradient, any strain measure can be calculated. Here, we use the logarithmic or true strain E defined as

$$E = \ln U \,, \tag{9}$$

where U is the material stretch tensor given by

$$U = \sum_{i=1}^{3} \lambda_i \, \Lambda_i \otimes \Lambda_i \,, \tag{10}$$

and $\{\lambda_i^2, \Lambda_i, \, i = 1,2,3\}$ are the eigenvalues and eigenvectors of the right Cauchy–Green tensor C given by

$$C = U^2 = \langle F \rangle^T \langle F \rangle \,. \tag{11}$$

For reporting simulation strain results, including both SVE and DNS results (shown in "Simulation of a Tube with Side-Holes Loaded in Tension: Comparison of DNS and Macroscale Material Models" section), we define an equivalent logarithmic strain $\bar{\varepsilon}$ as

$$\bar{\varepsilon} \doteq \sqrt{\frac{2}{3} \; \text{dev} \; E : \; \text{dev} \; E} \,, \tag{12}$$

where $\text{dev} \; E = E - \left(\frac{1}{3} tr(E)\right) I$ is the deviatoric part of the strain tensor, $tr(\cdot)$ is the trace operator, and I is the identity tensor. The 2/3 factor gives consistency with the case of uniaxial loading in the plastic regime where Poisson's ratio is 1/2. For reporting simulation stress results, we use the von Mises equivalent stress σ_{VM} given by

$$\sigma_{VM} \doteq \sqrt{\frac{3}{2} \; \text{dev} \; \langle \sigma \rangle : \; \text{dev} \; \langle \sigma \rangle} \,. \tag{13}$$

The equivalent logarithmic strain fields for three SVE microstructural realizations, loaded in uniaxial stress, are shown in Fig. 6. Each SVE contains approximately 16^3 grains. The +3 mesh resolution was used in the simulations. The stress rate was 1 MPa/s with results shown corresponding to a volume-averaged stress of 400 MPa. Statically uniform

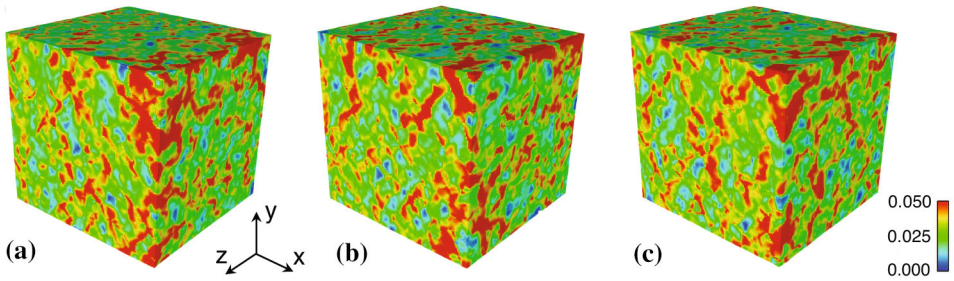

Fig. 6. Equivalent logarithmic strain fields for the three microstructural realizations (a)–(c) loaded uniaxially in stress control to a volume-averaged stress of 400 MPa. The stress rate was 1 MPa/s.

tractions were applied to the SVE in order to obtain a volume-averaged uniaxial stress state as described below.

A series of SVE simulations was conducted to choose an appropriate RVE size (number of grains) and mesh refinement level (+2, +3, or +4). Statically uniform tractions were applied at 1 MPa/s to the $+x$ face in the x direction of the SVE in order to obtain a volume-averaged uniaxial stress state. In order to increase the effective size of the SVE, symmetry boundary conditions were applied on the $-x$, $-y$, and $-z$ faces. The effect of SVE size on the stress–strain response is shown in Fig. 7 using the +3 mesh refinement. Results from three microstructural realizations are shown for each case. There is some variation in the results between the different realizations for the 4^3 grain case, but very little scatter in the results for 8^3 grains. The case of 16^3 has no discernible scatter and is effectively deterministic. Thus, we assign a minimum RVE size as a volume containing approximately 16^3 grains.

The effect of mesh refinement (+2, +3, and +4) on the stress–strain response of an SVE is shown in Fig. 8 for three SVE sizes: (a) 4^3 grains, (b) 8^3 grains, and (c) 16^3 grains. Each SVE is loaded in uniaxial tension. Results from one microstructural realization are shown for each case. There is some sensitivity to mesh refinement for each SVE size. The largest change is seen between the +2 and +3 mesh refinements. As a compromise between the competing goals of mesh-independent results and maximizing the number of grains modeled with a given mesh, the +3 mesh refinement will be used in all remaining RVE and DNS analyses.

Strain-Rate Sensitivity

In order to understand the strain-rate sensitivity of the polycrystalline material, several RVE simulations were performed in strain control at three engineering strain rates, 5×10^{-5}/s, 5×10^{-4}/s, and 5×10^{-3}/s. The stress–strain results are shown in Fig. 9. Results from three microstructural realizations are shown for each strain rate, with no observable scatter in the results. There is minor strain-rate dependence evident in the results. For the macroscale plasticity model, we could use a strain-rate dependent hardening model such as the Johnson–Cook model[55] or we could use a viscoplastic constitutive model.[56] Since the observed strain-rate dependence is small, we instead use a rate-independent macroscale plasticity model. This approximation is another type of model-form error.

As noted previously, all stress-controlled SVE/RVE simulations in this work have been performed at a stress rate of 1 MPa/s. For the hardening behavior exhibited by the polycrystalline material, this stress rate is approximately equal to a strain rate of 5×10^{-4}/s.

Calibration of Macroscale Plasticity Models

The Hosford family of isotropic yield surfaces is defined by the implicit surface

$$f(\sigma, \bar{\varepsilon}^p) = \phi(\sigma) - \sigma_y(\bar{\varepsilon}^p) = 0 \tag{14}$$

where $\sigma_y(\bar{\varepsilon}^p)$ is the hardening function, $\bar{\varepsilon}^p$ is the equivalent plastic strain defined in Eq. 23, and $\phi(\sigma)$ is the Hosford effective stress given by[57]

$$\phi(\sigma) = \left\{ \frac{1}{2} \left(|\sigma_1 - \sigma_2|^a + |\sigma_1 - \sigma_3|^a + |\sigma_2 - \sigma_3|^a \right) \right\}^{1/a}, \tag{15}$$

where σ_1, σ_2, and σ_3 are the principal stresses, and $a \in [1, \infty)$ is a material parameter. For a given yield surface, the value of a is not unique. Multiple values of a can correspond to the same yield surface. The cases $a = 2$ and $a = 4$ correspond to the von Mises yield surface. The cases $a = 1$ and $a = \infty$ correspond to the Tresca yield surface. For $a \in (1, 4)$ and $a \in (4, \infty)$, the yield surface is between the Tresca and von Mises surfaces as illustrated by $a = 8$ in Fig. 10.

A numerical implementation of the Hosford plasticity algorithm provided by Scherzinger[57] is used here. The algorithm assumes associated flow so that the plastic flow direction is given by the normal to the yield surface. We also assume isotropic hardening in stress space so that the yield surface hardens proportionally along all possible stress paths.

In order to define the hardening response $\sigma_y(\bar{\varepsilon}^p)$ of an RVE, we first need to recover the plastic strain. To this end, we additively partition the strain E into

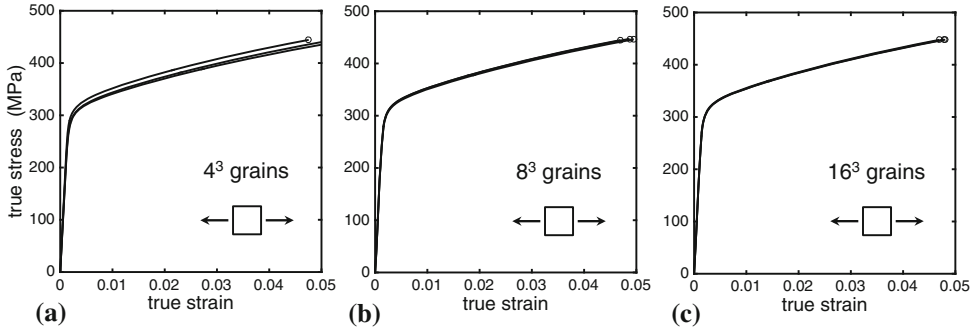

Fig. 7. Stress versus strain of an SVE loaded in uniaxial tension showing the effect of SVE size (number of grains): (a) 4^3 grains, (b) 8^3 grains, and (c) 16^3 grains. Results from three microstructural realizations are shown for each case. The +3 mesh refinement is used. The SVEs are loaded at a stress rate of 1 MPa/s. (The *symbol* denotes the end of the simulation resulting from either completion of the loading or numerical difficulties in the crystal-plasticity algorithm due to locally high deformation near the surface of the SVE).

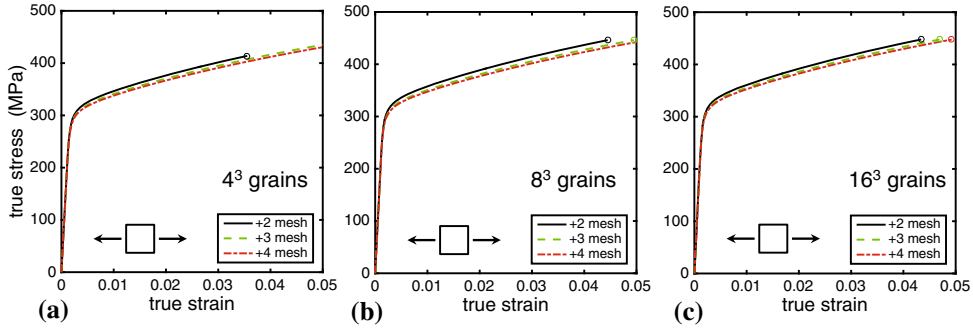

Fig. 8. Effect of mesh refinement (+2, +3, and +4) on the stress–strain response of SVEs loaded in uniaxial tension for three SVE sizes: (a) 4^3 grains, (b) 8^3 grains, and (c) 16^3 grains. Results from one microstructural realization are shown for each case. The SVEs are loaded in stress control at a stress rate of 1 MPa/s.

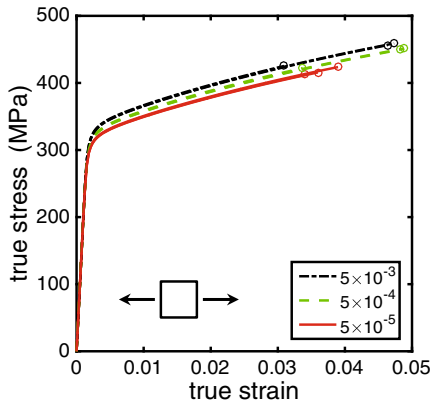

Fig. 9. Stress versus strain for an RVE loaded in strain control at three engineering strain rates, 5×10^{-3}/s, 5×10^{-4}/s, and 5×10^{-5}/s. Results from three microstructural realizations are shown for each strain rate. (Each RVE contains approximately 16^3 grains, +3 mesh refinement. The *symbol* denotes the end of the simulation).

elastic E^e and plastic E^p components. In elastoplasticity, it is customary to assume that the total deformation gradient F can be decomposed into elastic F^e and plastic components F^p so that,

$$\langle F \rangle = F^e F^p \ . \tag{16}$$

Then,

$$U^2 = \langle F \rangle^T \langle F \rangle = (F^p)^T (F^e)^T F^e F^p \ = (F^p)^T (U^e)^2 F^p$$
$$= (U^p)^T (U^e)^2 U^p \ . \tag{17}$$

In the RVE simulations used in this work, the loading is applied in principal stress directions (no shear loading). Also, the strain derived from the volume-averaged deformation gradient (Eq. 9) is less than 5%, so that minimal texture is developed during deformation. We approximate the homogenized elasticity tensor as being constant during deformation. We also assume that the effective macroscale plastic response remains isotropic. It follows that U^e and U^p are diagonal, and thus commute, so that

$$U^2 = (U^e)^2 (U^p)^2 \ . \tag{18}$$

Taking the matrix logarithm of both sides gives

$$\ln U = \ln U^e + \ln U^p \ , \tag{19}$$

so that

$$E = E^e + E^p \ . \tag{20}$$

We obtain the RVE-level elastic strain tensor E^e directly from the RVE-averaged Cauchy stress tensor,

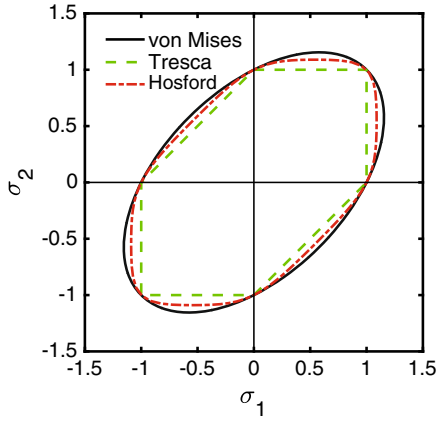

Fig. 10. Comparison of yield surfaces in plane stress: von Mises, Tresca, and Hosford ($a = 8$).

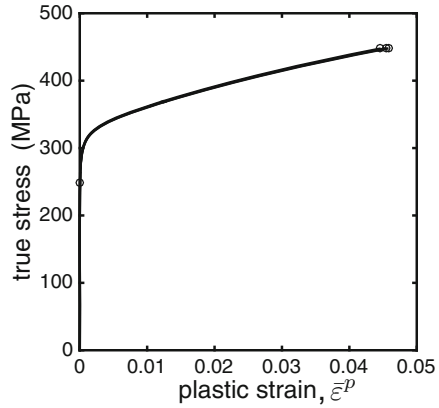

Fig. 11. Stress versus plastic strain for an RVE loaded in uniaxial tension. Results from three microstructural realizations are shown. This hardening response is used in both the von Mises and Hosford macroscale plasticity models. (stress rate = 1 MPa/s, approximately 16^3 grains, +3 mesh refinement).

$$E^e = S^{iso}\langle\sigma\rangle \,, \tag{21}$$

where S^{iso} is the isotropic compliance tensor obtained in.[10] Then,

$$E^p = E - S^{iso}\langle\sigma\rangle \,. \tag{22}$$

Finally, an equivalent plastic strain $\bar{\varepsilon}^p$ is defined as usual,[7]

$$\bar{\varepsilon}^p \doteq \sqrt{\frac{2}{3}E^p : E^p} \,. \tag{23}$$

Figure 11 shows the stress versus plastic strain for an RVE loaded in uniaxial tension. A stress value of 250 MPa was assigned as the proportional limit (onset of plastic strain) for the RVE. This hardening response $\sigma_y(\bar{\varepsilon}^p)$ is used for both the von Mises and Hosford macroscale plasticity models.

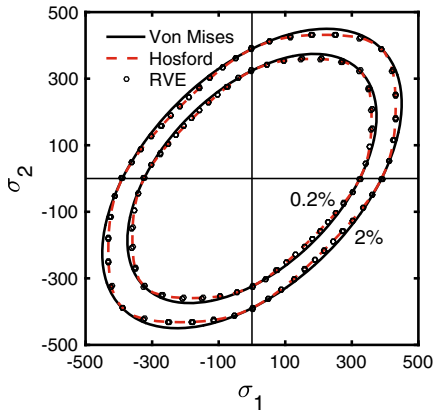

Fig. 12. Plane-stress yield surface of the polycrystalline material (RVE) at equivalent plastic strain values of 0.2% and 2.0%. Results from three microstructural realizations are shown. The calibrated Von Mises yield surface ($a = 2$ or $a = 4$) and Hosford yield surface ($a = 1.49$ or $a = 6.53$) are also shown. (Stress values are in MPa, von Mises equivalent stress rate = 1 MPa/s, approximately 16^3 grains, +3 mesh refinement).

The yield surface, in plane stress, of the polycrystalline material (RVE) is shown in Fig. 12 for equivalent plastic strain values of 0.2% and 2.0%. Results from three RVE microstructural realizations are shown at discrete values of the stress ratio σ_2/σ_1. The biaxiality angle $\theta = \tan^{-1}\sigma_2/\sigma_1$ is varied by increments of 7.5° starting at $\theta = -45°$ and stopping at $\theta = 45°$. Symmetry conditions were used to construct the remainder of the yield surfaces. The von Mises yield surface is also shown. Note that the difference in the yield surface of the RVE and the von Mises yield surface in the biaxial loading conditions $\sigma_2 = -\sigma_1$ and $\sigma_2/\sigma_1 = \tan 30°$.

To calibrate the Hosford yield surface, we use two of the flow stress values reported in Fig. 12 at an equivalent plastic strain of $\bar{\varepsilon}^p = 0.2\%$. For $\sigma_2 = 0$, $\sigma_1 = 326$MPa. For $\sigma_2/\sigma_1 = \tan 30°$, $\sigma_2 = 208$MPa. Using these values in Eq. 15 gives the following equation for the parameter a,

$$(\sqrt{3}-1)^a + (\sqrt{3})^a - 2(1.565)^a + 1 = 0 \,. \tag{24}$$

Using the secant method of root finding with $a \in [1, 2]$ we obtain $a = 1.49$. This value of a is not unique. For the range $a \in [4, \infty)$, we obtain equivalently $a = 6.53$. The identified Hosford yield surface is shown in Fig. 12. This yield surface fits the RVE biaxial response very well for both $\bar{\varepsilon}^p = 0.2\%$ and $\bar{\varepsilon}^p = 2.0\%$.

Figure 13 compares the stress–strain response of an RVE and the calibrated von Mises and Hosford macroscale plasticity models for three biaxial stress states: (a) uniaxial tension, (b) $\sigma_2/\sigma_1 = \tan 30°$, and (c) $\sigma_2/\sigma_1 = -1$. For the RVE, three microstructural realizations are shown. The equivalent stress is the Mises equivalent stress σ_{VM}, and the equivalent strain $\bar{\varepsilon}$ was defined in Eq. 12. There is some error

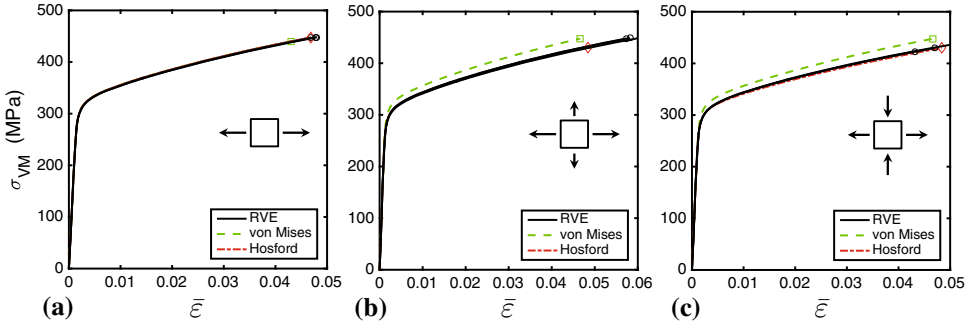

Fig. 13. Comparison of the stress–strain response of an RVE and the calibrated macroscale plasticity models (von Mises and Hosford) for three stress conditions: (a) uniaxial tension, (b) biaxial loading with $\sigma_2/\sigma_1 = \tan 30^\circ$, and (c) biaxial loading with $\sigma_2/\sigma_1 = -1$. The von Mises equivalent stress σ_{VM} and equivalent logarithmic strain $\bar{\varepsilon}$ are used. (For the RVE, three microstructural realizations are shown, Mises equivalent stress rate = 1 MPa/s, approximately 16^3 grains, +3 mesh refinement).

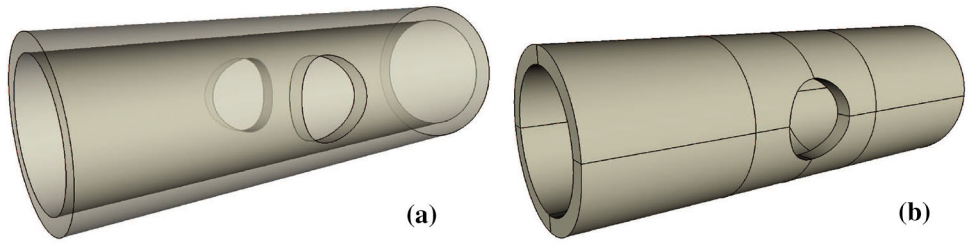

Fig. 14. (a) Example macroscale structure, a tube with side-holes. (b) Decomposition of the tube into subregions for hexahedral meshing.

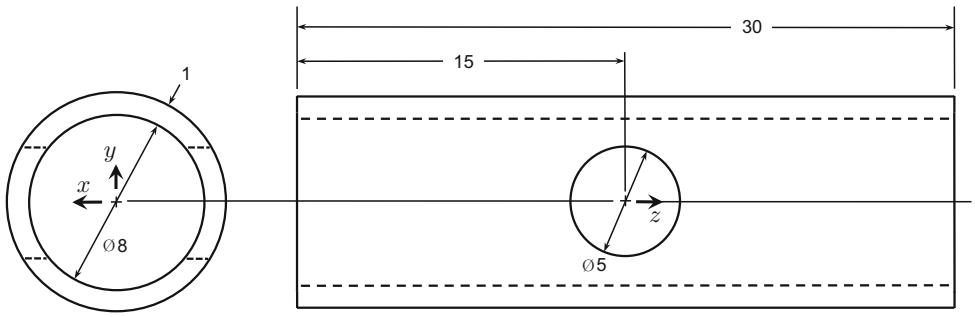

Fig. 15. Dimensions of the example macroscale structure, a tube with side-holes. A rectilinear coordinate system (*x y z*) is identified.

evident in the von Mises plasticity model, whereas the calibrated Hosford model shows little error in the stress–strain response.

SIMULATION OF A TUBE WITH SIDE-HOLES LOADED IN TENSION: COMPARISON OF DNS AND MACROSCALE MATERIAL MODELS

The example macroscale structure is a tube with side-holes as shown in Fig. 14. The tube is loaded quasi-statically in tension into the plastic regime. Additional analysis of the tube loaded non-proportionally in tension–torsion will be the subject of a future communication. The dimensions of the tube and definition of the loading are given in "Tube Geometry and Loading" section. Details of the hexahedral meshing are given in "Tube Meshing" section. The embedded microstructure is shown in "Embedded Microstructure" section. DNS stress and strain results are given in "Stress and Strain Results" section for three microstructure realizations. These results are then compared to results obtained using the macroscale elastic-plastic material models calibrated in "Macroscale Material Model" section.

Tube Geometry and Loading

The dimensions of the tube are given in Fig. 15 in nondimensional units. For specificity, we take the units to be millimeters, but only the size of the tube

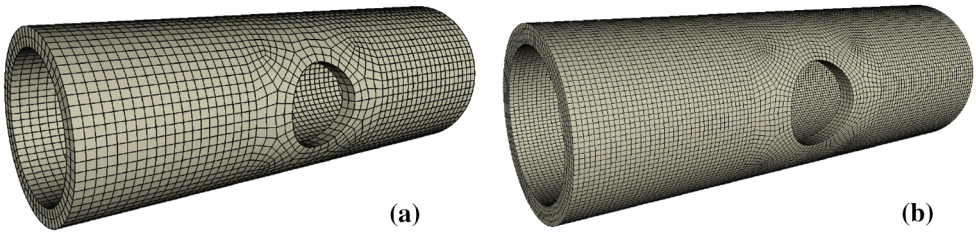

Fig. 16. (a) The base hexahedral mesh of the tube, denoted as $r0$, contains 7232 hexahedra. Subsequent hexahedral meshes, $r1$, $r2$, $r3$, $r4$, and $r5$ are obtained from uniform hierarchical refinement in which each hexahedral element is divided into eight elements. New surface nodes created during each refinement are located on the exact geometry. (b) The refinement $r1$ contains approximately 57,900 hexahedra. Subsequent refinements $r2$, $r3$, $r4$, and $r5$ (not shown) contain approximately 463,000, 3.70 million, 29.6 million, and 237 million hexahedra, respectively.

relative to the size of the grain structure is significant. (Recall that the crystal-plasticity model described in "Crystal-Plasticity Model" section has no inherent length scale.) This ratio will be denoted throughout as the "thickness-to-grain ratio." The tube is 30 mm long and the thickness is 1 mm. The volume of the tube is approximately 807 mm^3.

To apply tension loading, equal and opposite surface tractions are applied at both end-surfaces of the tube ($z = -15$ and $z = 15$). The traction vectors are given by

$$\left.\begin{aligned} T_x &= 0 \\ T_y &= 0 \\ T_z &= -T_0\,(t/t_0) \end{aligned}\right\} \text{ at } z = -15\,, \quad \text{and}$$
$$\left.\begin{aligned} T_x &= 0 \\ T_y &= 0 \\ T_z &= T_0\,(t/t_0) \end{aligned}\right\} \text{ at } z = 15\,, \tag{25}$$

where $T_0 \doteq 200$ is a traction scale factor, $t \in [0, 200]$ is a time variable, and $t_0 \doteq 200$ is a time constant. Thus, the stress rate (uniaxial) in the tube (away from the hole) is 1 MPa/s. Based on the macroscale plasticity models identified in "Macroscale Material Model" section, the resulting strain rates are on the order of 10^{-4}/s.

Tube Meshing

The meshing software CUBIT[29] was used to create both the geometry and mesh of the tube. In order to mesh the tube with hexahedra, it was first partitioned as shown in Fig. 14b. The multiple symmetry plains of the tube were exploited so that only two subregions needed to be meshed. The remaining regions were meshed through simple reflections. The base hexahedral mesh of the tube is shown in Fig. 16a. This base mesh, denoted by $r0$, contains 7232 hexahedra with 2 hexahedra through the wall thickness of the tube. Subsequent hexahedral meshes, $r1$, $r2$, $r3$, $r4$, and $r5$ were obtained from uniform hierarchical refinement in which each hexahedron was divided into eight. New surface nodes created during each refinement were located on the exact geometry. The $r1$ mesh refinement is shown in Fig. 16b and contains 57,856 hexahedra. The mesh refinements $r2$, $r3$, $r4$, and $r5$ contain approximately 463,000, 3.70 million, 29.6 million, and 237 million hexahedra, respectively. The $r4$ mesh refinement is used in the actual simulations of the tube under applied loading.

Embedded Microstructure

The model microstructure defined in "Microstructural Model" section is embedded into the macroscale tube structure using the DNS methodology described in "Direct Numerical Simulation" section. We use a grain size resulting in approximately four grains through the tube thickness and the $r4$ hexahedral mesh refinement. For a tube thickness of 1 mm, this implies that the grain size is approximately 250 μm. (This is admittedly a rather large grain size. The grain size in wrought AISI 304L stainless steel is typically < 100 μm, depending upon the processing history of the material (see Fig. 4a). This level of mesh refinement in the tube results in a $+3$ mesh resolution of each grain, or about 8^3 hexahedral elements per grain. This resolution is consistent with the RVE homogenization procedure discussed in "Macroscale Material Model" section. A realization of the microstructure with this grain size is shown in Fig. 17a, b. The total number of grains for this realization is approximately 51,000. An end view of the tube is also shown.

A microstructural realization with approximately eight grains through the web-section thickness using the $r5$ mesh refinement is shown in Fig. 17c and d. For a web-section thickness of 1 mm, this implies that the grain size is approximately 125 μm. The total number of grains for this realization is approximately 358,000. The analysis of this smaller grain structure is the subject of an ongoing investigation.

Stress and Strain Results

As described in "Direct Numerical Simulation" section, the tube boundary-value problem is solved using the solid mechanics module within the Sierra multiphysics finite-element software suite[27] and the

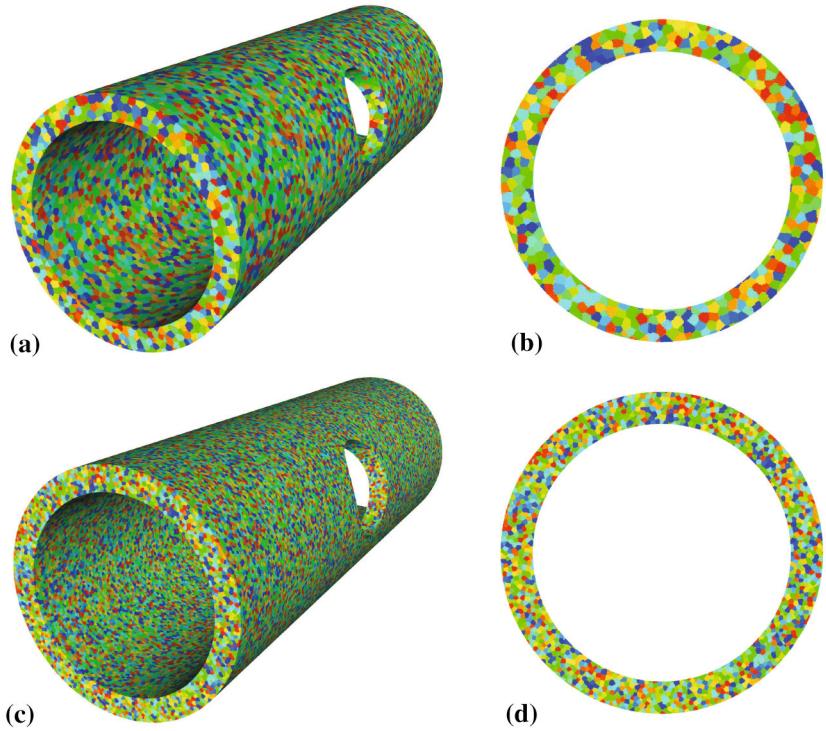

Fig. 17. (a) Tube with embedded microstructure with approximately four grains through the tube thickness, i.e., thickness-to-grain ratio = 4. The total number of grains for this realization of the microstructure is approximately 51,000. (The *r*4 hexahedral mesh refinement containing 29.6 million elements is used.) (b) An end view of the tube. (c) Tube with embedded microstructure with approximately 8 grains through the tube thickness, i.e., thickness-to-grain ratio = 8. The total number of grains for this realization of the microstructure is approximately 358,000. (The *r*5 hexahedral mesh refinement containing 237 million elements is used.) (d) An end view of the tube. (The color of each grain is arbitrary, and does not indicate crystal orientation).

FETI-DP domain-decomposition iterative solver.[28] The hexahedral finite-element formulation used selectively deviatoric integration for the DNS simulations. For each microstructural realization using the *r*4 mesh refinement (containing 29.6 million elements), 2400 processors were used with typical runtimes of approximately 4 days.

The von Mises stress and equivalent logarithmic strain fields resulting from the direct numerical simulation of the tube are shown in Fig. 18a and b, respectively. The microstructure is shown in Fig. 17a. The element stress and strain values resulting from the finite-element analysis are shown with no smoothing or other post-processing. Top views of the tube (*y*-direction) are shown in Figs. 19 and 20 along with results from two additional microstructural realizations. The results for each microstructural simulation are qualitatively similar in their overall distribution but distinctly different at the fine scale.

The von Mises stress field and equivalent logarithmic strain field in the tube resulting from the tension loading using the homogeneous macroscale von Mises plasticity model are shown in Fig. 18c and d, respectively. The element-stress values resulting from the finite-element analysis are shown with no smoothing or other post-processing. The stress and strain fields resulting from the use of the Hosford plasticity model (not shown) are qualitatively similar. The DNS fields display large fluctuations on small spatial scales, but are qualitatively similar to the smooth fields obtained by using the macroscale plasticity models. The fine-scale fluctuations are effectively filtered out in the homogeneous macroscale solution. The top views of these results are shown in Figs 19d and 20d.

In order to investigate the differences between the DNS and macroscale plasticity models, the stress and strain magnitudes along two curves/lines within the tube are extracted and graphed. These extraction curves are identified in Fig. 21. Extraction line 1 is discretized with 20,000 points, and extraction curve 2 is discretized with 10,000 points. For each point, the enclosing finite element is found, and a mean element stress (strain) tensor is assigned as the stress (strain) tensor at the given point. Figure 22 shows the equivalent strain $\bar{\varepsilon}$ and the von Mises stress σ_{VM} along the surface of the tube (line 1 identified in Fig. 21) extracted from the results shown in Figs. 19 and 20, respectively. Results obtained using the von Mises macroscale plasticity model are also shown. No smoothing operations are performed on the extracted stress and strain values. The smooth variation of the

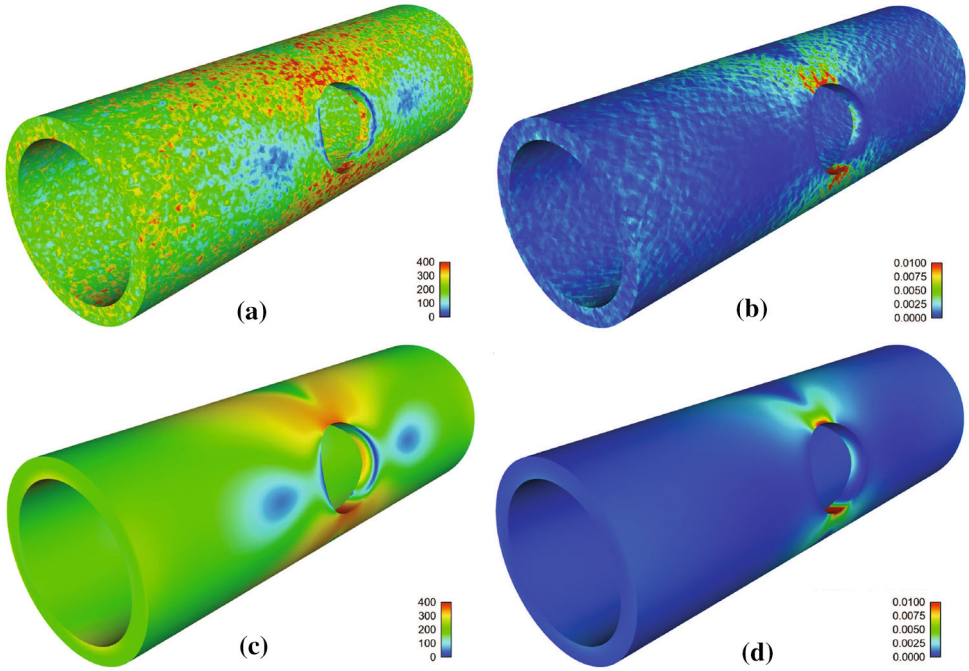

Fig. 18. (a) von Mises stress field and (b) equivalent logarithmic strain field resulting from the direct numerical simulation of the tube containing the microstructure shown in Fig. 17a loaded in uniaxial tension. (c) von Mises stress field and (d) equivalent logarithmic strain field resulting from using the homogeneous macroscale von Mises plasticity model. (Stress units are MPa).

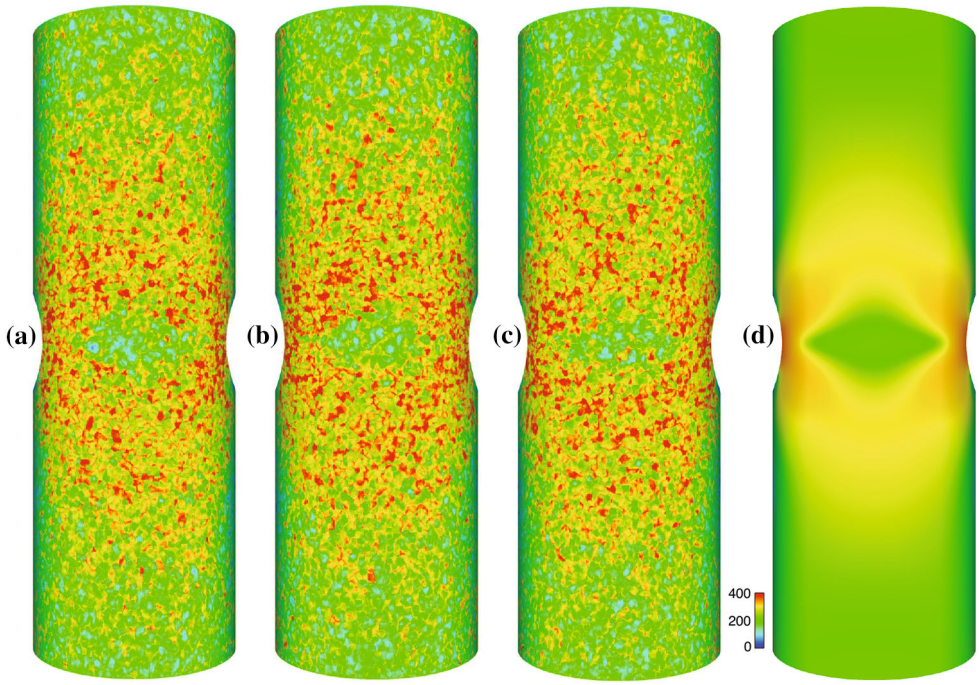

Fig. 19. von Mises stress field resulting from the direct numerical simulation of the tube containing the microstructure shown in Fig. 17a loaded in uniaxial tension. (a) Microstructural realization 1, (b) microstructural realization 2, (c) microstructural realization 3, (d) response using the homogeneous macroscale von Mises plasticity model. (Stress units are MPa).

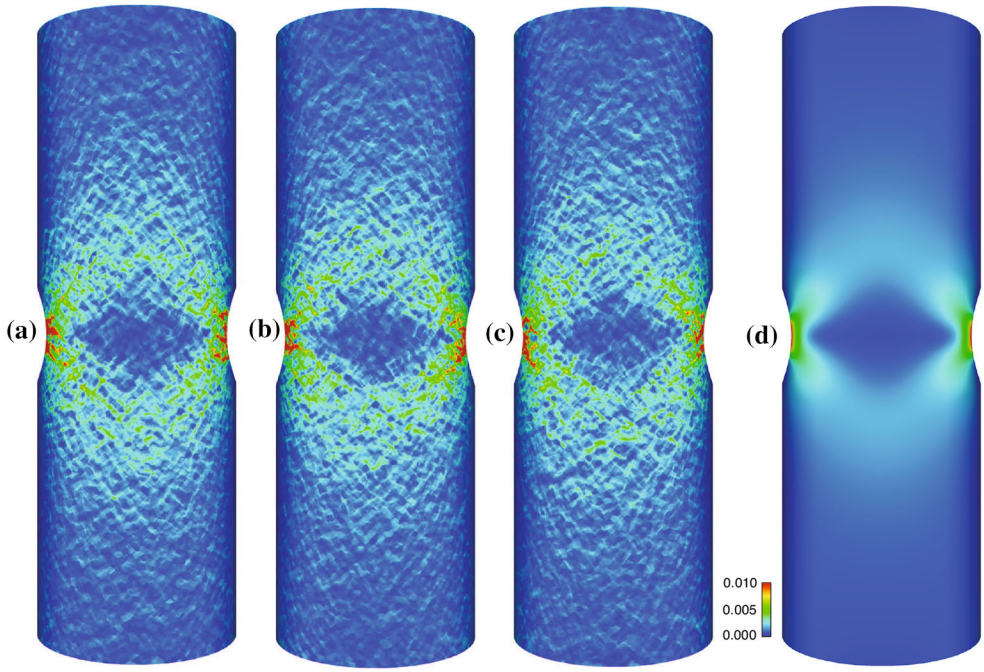

Fig. 20. Strain field (equivalent logarithmic) resulting from the direct numerical simulation of the tube containing the microstructure shown in Fig. 17a loaded in uniaxial tension. (a) Microstructural realization 1, (b) microstructural realization 2, (c) microstructural realization 3, (d) response using the homogeneous macroscale von Mises plasticity model.

homogeneous finite-element results is due to the extremely fine mesh refinement used in these simulations. Note that the homogeneous macroscale model gives perfectly symmetric results about the mid-section of the tube, whereas the DNS solutions are clearly unsymmetric. Also, the DNS results are clearly stochastic, whereas the homogeneous macroscale models are deterministic. The von Mises macroscale plasticity model reasonably approximates the mean-field DNS stress results, but underpredicts the mean-field DNS equivalent-strain results by approximately 20%. Further analysis of the DNS results using spatial filtering techniques, such as a moving volume-average,[10] can be used to obtain the low spatial frequency component of the DNS results.

The difference between strain results from the DNS simulations and the von Mises macroscale plasticity simulations possibly results from several factors. First, and foremost, the grain size in the DNS simulations is relatively large, only four grains through the tube cross-section. First-order homogenization theory assumes that the grain size is much smaller than the characteristic length scale in the macroscale structure. Second, homogenization theory predicts the existence of a surface effect due to the difference in confinement in the bulk material versus the surface.[58,59] The extraction lines are on the surface of the tube. Third, the von Mises plasticity model provides only an approximation to the macroscale response, as evidenced by Figs. 12 and 13.

In general, the error in stress or strain at a point in a body is due to both the material model error at that point (local error) in addition to pollution error propagating from the rest of the domain. In order to investigate the local error, Fig. 23a shows the two non-zero stress components, σ_{xx} and σ_{zz}, along the extraction line 1. Due to symmetry, and the fact that extraction line 1 is on the surface of the tube, these two stress components are principal stresses. The other principal stress is zero. It is interesting that the stress state is significantly biaxial away from the stress concentrations caused by the two holes. The stress biaxiality angle, $\theta = \tan^{-1} \sigma_{xx}/\sigma_{zz}$, is shown in Fig. 23b. Even though the tube is loaded uniaxially, significant biaxiality occurs throughout the tube. Thus, we expect the Hosford macroscale plasticity model to give more accurate results (see Fig. 12). Figure 24 compares the von Mises macroscale plasticity model results to those from the Hosford macroscale plasticity model. Surprisingly, the results differ by less than 3%, for both equivalent strain and von Mises stress. Greater differences in the macroscale results provided by the von Mises and Hosford plasticity models are expected if the tube were loaded in torsion or combined tension–torsion, and to larger strains.

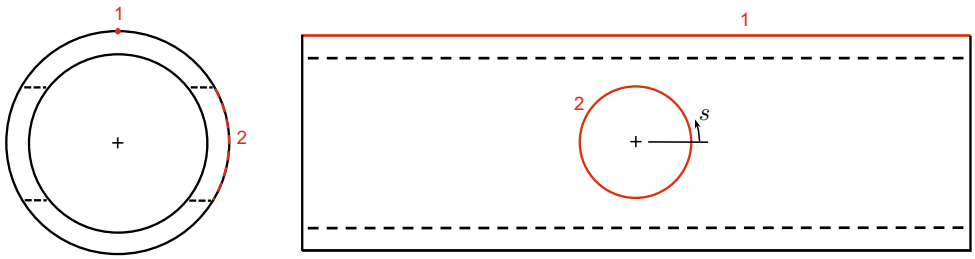

Fig. 21. Stress and strain results in the tube are extracted along two lines/curves: (1) *Line 1* is along the outside length of the tube with start and endpoints $(0, 5, -15)$ and (0, 5, 15), respectively. (2) *Curve 2* is along the outer edge of the side hole on the $-x$ side. A circumferential coordinate, s, is also defined.

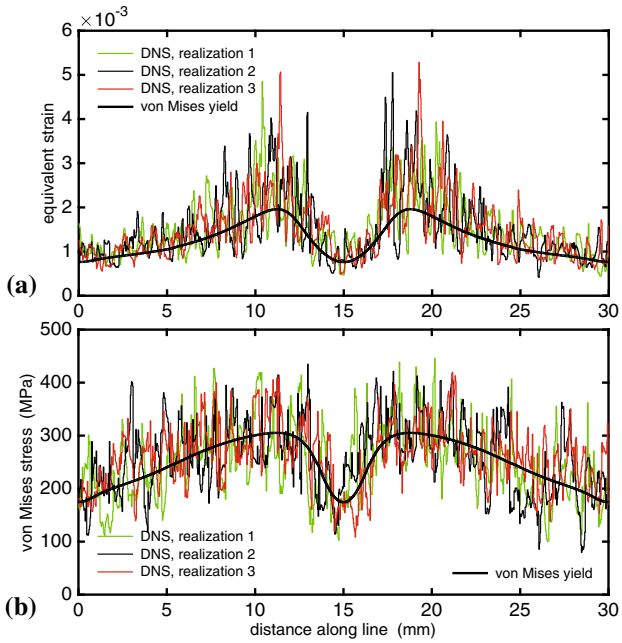

Fig. 22. (a) Equivalent strain $\bar{\varepsilon}$ and (b) von Mises stress σ_{VM} along the surface of the tube (line 1 identified in Fig. 21) extracted from the DNS results shown in Figs. 19 and 20, respectively. Results obtained using the von Mises macroscale plasticity model are also shown.

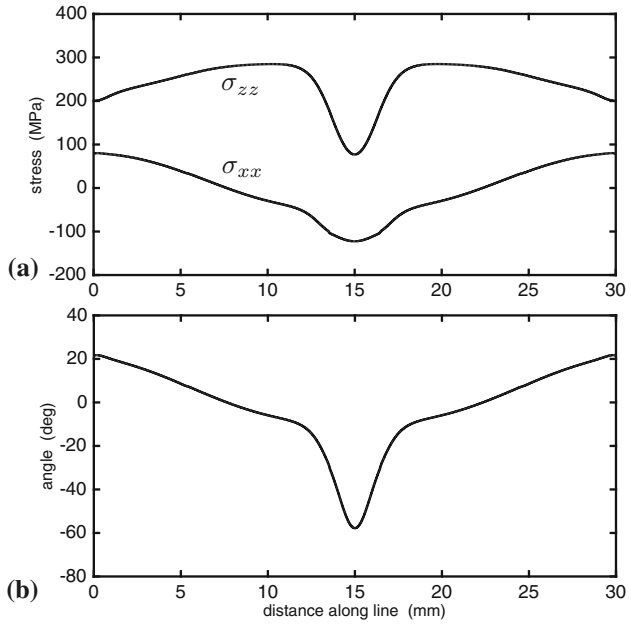

Fig. 23. (a) Stress components σ_{xx} and σ_{zz} along the surface of the tube (line 1 identified in Fig. 21) extracted from the von Mises macroscale plasticity model results shown in Figs. 19d. (b) Stress biaxiality angle, $\theta = \tan^{-1} \sigma_{xx}/\sigma_{zz}$.

Analogous results to those shown in Fig. 22, but around the edge of the hole (curve 2 identified in Fig. 21), are shown in Fig. 25. Again, results from the homogeneous macroscale von Mises model are perfectly symmetric, whereas the DNS solutions are clearly unsymmetric and stochastic. The von Mises macroscale plasticity model reasonably approximates the mean-field DNS stress results, but underpredicts the mean-field DNS equivalent-strain results by approximately 30%. Figure 26 compares the von Mises macroscale plasticity model results to those from the Hosford macroscale plasticity model. The stress results differ by less than 3%, and the equivalent strain results differ by less than 12%. Note that the extraction curve 1 lies on the edge of the hole, and thus experiences an approximately uniaxial stress state, since two of the principal stresses are nearly zero. Thus, the stress state along the edge of the curve is very near the uniaxial calibration point of the two plasticity models, and any observed differences in results from the two models must be due to pollution error.

The total load applied to the tube versus the resulting stretch of the tube is shown in Fig. 27 for the three DNS realizations. There is no observable scatter in the results. The results are essentially deterministic. Results obtained using the von Mises and Hosford macroscale plasticity models are also shown. There is some difference observed between the DNS results and the macroscale plasticity models, less than 5%. There is no observable difference between the von Mises and Hosford model results. Larger differences are expected in torsional or combined tension–torsion loading and for larger macroscopic strains.

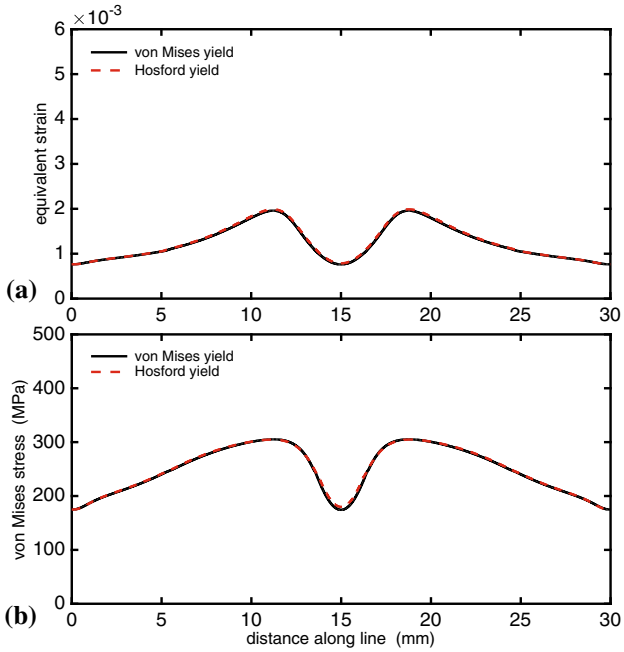

Fig. 24. Comparison of simulation results from the von Mises and Hosford macroscale plasticity models. (a) Equivalent strain $\bar{\varepsilon}$ and (b) von Mises stress σ_{VM} along the surface of the tube (line 1 identified in Fig. 21).

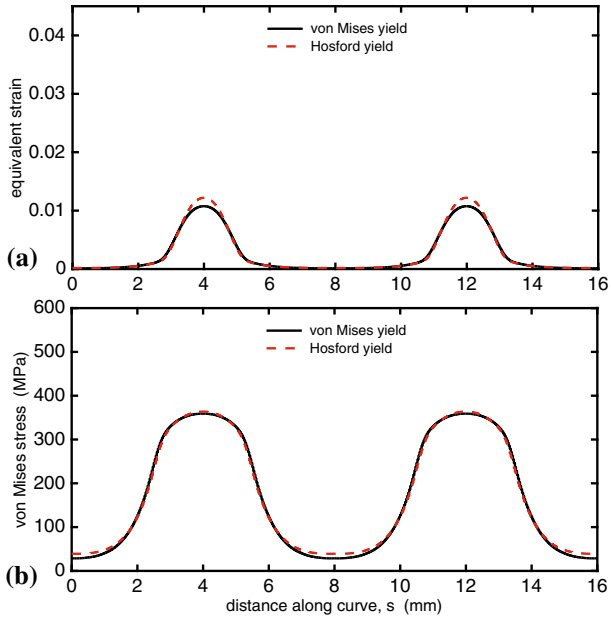

Fig. 26. Comparison of simulation results from the von Mises and Hosford macroscale plasticity models. (a) Equivalent strain $\bar{\varepsilon}$ and (b) von Mises stress σ_{VM} along the surface of the tube (curve 2 identified in Fig. 21).

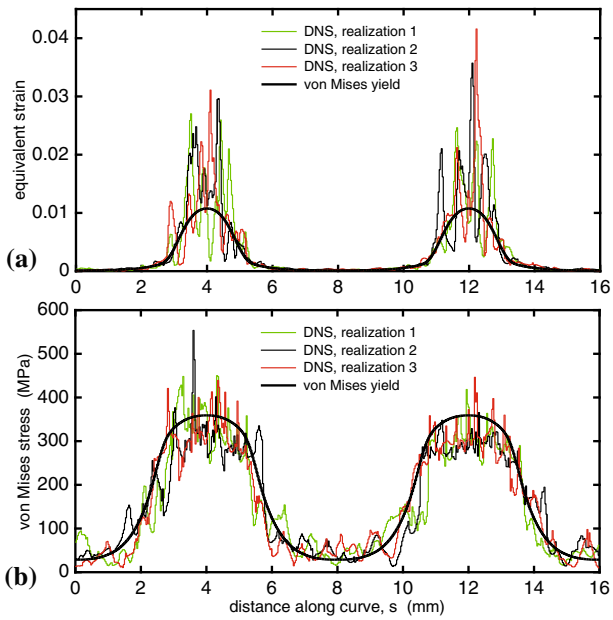

Fig. 25. (a) Equivalent strain $\bar{\varepsilon}$ and (b) von Mises stress σ_{VM} along the surface of the tube (curve 2 identified in Fig. 21) extracted from the DNS results shown in Figs. 19 and 20, respectively. Results obtained using the von Mises macroscale plasticity model are also shown.

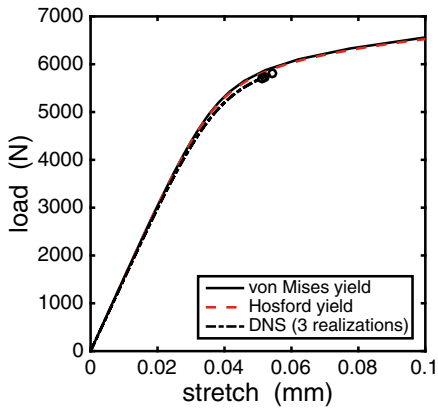

Fig. 27. Total load applied versus stretch of the tube for three DNS realizations. Results obtained using the macroscale von Mises and Hosford plasticity models are also shown. (The *symbols* denote the end of the DNS simulation results, due to compute time limitations).

CONCLUSION

Two fundamental approximations in macroscale solid-mechanics modeling are (1) the assumption of scale separation in homogenization theory and (2) the use of a macroscopic plasticity material model

that represents, in a mean sense, the inelastic processes occurring at the microscale. With the goal of quantifying the macroscale errors induced by these approximations, we performed a set of direct numerical simulations (DNS) in which polycrystalline microstructures were embedded throughout a macroscale structure.

The stochastic results from the DNS simulations were compared to the deterministic results obtained from conventional macroscale simulations. The homogeneous macroscale simulations used the von Mises and Hosford isotropic plasticity models calibrated using a representative volume element (RVE). The Hosford plasticity model matched the RVE response in the multiaxial regime significantly better than the von Mises plasticity model, even though both plasticity models used the same hardening curve. Both macroscale plasticity models provided a good approximation to the spatial mean of the DNS *stress* field. However, both models underpredicted the spatial mean of the DNS *strain* field. The Hosford plasticity model was slightly more accurate than the von Mises plasticity model. Greater differences in the macroscale results provided by the von Mises and Hosford plasticity models are expected if the tube were loaded in torsion or combined tension–torsion, and to larger strains.

The observed large fluctuations in the microscale stress and strain fields reinforce the importance of microstructural effects in predicting fatigue and fracture initiation. Furthermore, the detailed DNS simulation results, unlike homogeneous macroscale simulations, can now be studied using modern data-science techniques, such as pattern recognition, for identifying emergent phenomena such as precursors to material failure. Ultimately, we envision that DNS modeling will be used to gain new insights into the mechanics of material deformation and failure.

ACKNOWLEDGEMENT

We would like to thank Ben Reedlunn for suggesting that we explore the use of the Hosford yield criteria. Also, we would like to thank Bill Scherzinger for the implementation of the Hosford plasticity algorithm within the Sierra finite-element software and discussions of its use. Sandia National Laboratories is a multi-program laboratory operated by Sandia Corporation, a wholly owned subsidiary of Lockheed Martin Corporation, for the US Department of Energy's National Nuclear Security Administration under contract DE-AC04-94AL85000.

REFERENCES

1. U. Kocks, C. Tome, and H. Wenk (eds.), *Texture and Anisotropy: Preferred Orientations in Polycrystals and their Effect on Material Properties* (Cambridge University Press, New York, 1998).
2. F. Roters, P. Eisenlohr, T. Bieler, and D. Raabe, *Crystal Plasticity Finite Element Methods: in Materials Science and Engineering* (Wiley, Berlin, 2010).
3. W. Frazier, *J. Mater. Eng. Perform.* **23**, 1917 (2014).
4. K. Vemaganti and T. Oden, *Comput. Methods Appl. Mech. Eng.* **190**, 6089 (2001).
5. A. Romkes, T. Oden, and K. Vemaganti, *Mech. Mater.* **38**, 859 (2006).
6. I. Temizer and P. Wriggers, *Comput. Methods Appl. Mech. Eng.* **200**, 2639 (2011).
7. J. Lubliner, *Plasticity Theory, Chap. 3.3* (Macmillan, New York, 1990).
8. W. Hosford, *J. Appl. Mech.* **39**, 607 (1972).
9. J. Vetter (ed.), *Contemporary High Performance Computing: From Petascale to Exascale* (Chapman and Hall/CRC, New York, 2013).
10. J. Bishop, J. Emery, R. Field, C. Weinberger, and D. Littlewood, *Comput. Methods Appl. Mech. Eng.* **287**, 262 (2015).
11. V. Tikare, E. Homer, E. Hernandez-Rivera, J. Madison, E. Holm, and B. Patterson, Hybrid models for the simulation of microstructural evolution influenced by coupled, multiple physical processes, Technical Report SAND2013-8440, Sandia National Laboratories, 2013.
12. S. Lee, G. Rohrer, and A. Rollett, *Modell. Simul. Mater. Sci. Eng.* **22**, 025017 (2014).
13. M. Ebeida, S. Mitchell, A. Patney, A. Davidson, and J. Owens, *Comput. Graph. For.* **31**, 785 (2012).
14. L. Li, L. Shen, and G. Proust, *Int. J. Num. Methods Eng.* **103**, 144 (2015).
15. A. Maniatty and P. Dawson, *Int. J. Num. Methods Eng.* **35**, 1565 (1992).
16. K. Matouš and A. Maniatty, *Int. J. Num. Methods Eng.* **60**, 2313 (2004).
17. Y. Zhang, T. Hughes, and C. Bajaj, *Comput. Methods Appl. Mech. Eng.* **199**, 405 (2010).
18. J. Qian, Y. Zhang, W. Wang, A. Lewis, M. Qidwai, and A. Geltmacher, *Int. J. Num. Methods Eng.* **82**, 1406 (2010).
19. C. Wang, *Modell. Simul. Mater. Sci. Eng.* **39**, 35 (2007).
20. C. Battaile, J. Emery, L. Brewer, and B. Boyce, *Philos. Mag.* **95**, 1069 (2015).
21. H. Lim, R. Dingreville, L. Deibler, T. Buchheit, and C. Battaile, *Comput. Mater. Sci.* **117**, 437 (2016).
22. R. Quey, P. Dawson, and F. Barbe, *Comput. Methods Appl. Mech. Eng.* **200**, 1729 (2011).
23. H. Lim, F. Abdeljawad, S. Owen, B. Hanks, J. Foulk, and C. Battaile, *Modell. Simul. Mater. Sci. Eng.* (2016, accepted).
24. T. Kanit, S. Forest, I. Galliet, V. Mounoury, and D. Jeulin, *Int. J. Solids Struct.* **40**, 3647 (2003).
25. P. Eisenlohr, M. Diehl, R. Lebenshohn, and F. Roters, *Int. J. Plast.* **46**, 37 (2013).
26. D. Pyle, J. Lu, D. Littlewood, and A. Maniatty, *Comput. Mech.* **52**, 135 (2013).
27. SIERRA Solid Mechanics Team, Sierra/SolidMechanics 4.36 User's Guide, SAND report SAND2015-2199, Sandia National Laboratories, Albuquerque, NM and Livermore, CA, 2015.
28. C. Farhat, M. Lesoinne, P. LeTallec, K. Pierson, and D. Rixen, *Int. J. Num. Methods Eng.* **50**, 1523 (2001).
29. CUBIT Geometry and Meshing Toolkit, Version 13.2, https://cubit.sandia.gov/public/13.2/Cubit-13.2-announcement.html, 2012.
30. Integrated computational materials engineering (ICME): Implementing icme in the aerospace, automotive, and maritime industries, The Minerals, Metals & Materials Society, http://www.tms.org/ICMEstudy, 2013.
31. N. Provatas and K. Elder, *Phase-Field Methods in Material Science and Engineering* (Wiley, Weinheim, 2010).
32. E. Holm and C. Battaile, *JOM* **53**, 20 (2001).
33. S. Plimpton, C. Battaile, M. Chandross, L. Holm, A. Thompson, V. Tikare, G. Wagner, E. Webb, and X. Zhou, Crossing the mesoscale no-man's land via parallel kinetic Monte Carlo, Technical Report SAND2009-6226, Sandia National Laboratories, 2009.
34. E. Lazar, J. Mason, R. MacPherson, and D. Srolovitz, *Acta Mater.* **59**, 6837 (2011).

35. J. Arvo, Fast random rotation matrices, in *Graphics Gems III*, ed. by D. Kirk (Academic, New York, 1992).
36. D. Rowenhorst, A. Rollett, G. Rohrer, M. Groeber, M. Jackson, P. Konijnenberg, and M. Graef, *Modell. Simul. Mater. Sci. Eng.* **23**, 083501 (2015).
37. H. Ledbetter, *Phys. Status Solidi A* **85**, 89 (1984).
38. M. Miller and P. Dawson, *J. Mech. Phys. Solids* **45**, 1781 (1997).
39. C. Gerard, B. Bacroix, M. Bornert, G. Cailletaud, J. Crepin, and S. Leclercq, *Comput. Mater. Sci.* **45**, 751 (2009).
40. C. Gerard, G. Cailletaud, and B. Bacroix, *Int. J. Plast.* **42**, 194 (2013).
41. V. Kouznetsova, W. Brekelmans, and F. Baaijens, *Comput. Mech.* **27**, 37 (2001).
42. M. Geers, V. Kouznetsova, and W. Brekelmans, *J. Comput. Appl. Math.* **234**, 2175 (2010).
43. D. Cioranescu and P. Donato, *An Introduction to Homogenization* (Oxford University Press, New York, 1999).
44. T. Tran, V. Monchiet, and G. Bonnet, *Int. J. Solids Struct.* **49**, 783 (2012).
45. V. Jikov, S. Kozlov, and O. Oleinik, *Homogenization of Differential Operators and Integral Functionals* (Springer, New York, 1994).
46. A. Bensoussan, J. Lions, and G. Papanicolaou, *Asymptotic Analysis for Periodic Structures* (American Mathematical Society, Providence, 2011).
47. X. Yin, W. Chen, A. To, C. McVeigh, and W. Liu, *Comput. Methods Appl. Mech. Eng.* **197**, 3516 (2008).
48. W. Drugan and J. Willis, *J. Mech. Phys. Solids* **44**, 497 (1996).
49. A. Gusev, *J. Mech. Phys. Solids* **45**, 1449 (1997).
50. M. Ostoja-Starzewski, *Int. J. Solids Struct.* **35**, 2429 (1998).
51. Z. Ren and Q. Zheng, *J. Mech. Phys. Solids* **50**, 881 (2002).
52. Z. Ren and Q. Zheng, *Mech. Mater.* **36**, 1217 (2004).
53. C. Huet, *J. Mech. Phys. Solids* **38**, 813 (1990).
54. S. Nemat-Nasser, *Mech. Mater.* **31**, 493 (1999).
55. G. Johnson and W. Cook, A constitutive model and data for metals subjected to large strains, high strain rates, and high temperatures. *7th International Symposium on Ballistics*, (The Hague, 1983), pp. 541–547.
56. D. Bammann, M. Chiesa, and G. Johnson, A state variable model for temperature and strain rate dependent metals, in *Constitutive Laws: Experiments and Numerical Implementation*, ed. A. Rajendran and R. Batra (The Hague, 1995), pp. 84.
57. B. Scherzinger, Sandia National Laboratories, Albuquerque, NM, unpublished research (2015).
58. H. Dumontet, *ESAIM Math. Modell. Numer. Anal.* **20**, 265 (1987).
59. J. Auriault and G. Bonnet, *Int. J. Eng. Sci.* **25**, 307 (1987).